JOURNAL OF MATERIALS SCIENCES 33 (1998) 2319–2330

Combustion synthesis and mechanical properties of molybdenum disilicide composites reinforced with SiC particulate

D. MANOMAISUPAT*, D. S. WILKINSON, A. PETRIC
Department of Materials Science and Engineering, McMaster University, Hamilton, Ontario, Canada L8S 4L7
E-mail: manomaisupat.ad926@hwcn.org

Intermetallic composites of molybdenum disilicide reinforced with silicon carbide were produced by combustion synthesis of the elemental powders. The combustion reaction was initiated near 700 °C and completed within a few seconds. The end product was a porous composite which was subsequently hot pressed to >97% theoretical density. The grains of the matrix were 8–14 μm in size surrounded by SiC particulate reinforcement of 1–5 μm. The mechanical properties of the composites improved with increasing SiC reinforcement. The hardness of the materials increased from 10.1 GPa to 12.7 GPa with the addition of 20 vol % SiC reinforcement, while the strength increased from 195 MPa to 299 MPa. The fracture toughness also increased from 2.79 MPa $m^{1/2}$ to 4.08 MPa $m^{1/2}$ with 20 vol % SiC.

1. Introduction

At present, there are few structural materials capable of operation above 1000 °C in an oxidizing environment. Nickel-based and titanium-based superalloys have been used successfully up to about 1000 °C, while silicon-based ceramics (SiC, Si_3N_4) and their composites are proposed for applications above 1000 °C. However, utilization of the ceramics has been hindered by various factors, such as their inherent brittleness over the entire operating temperature range and the high cost and difficulties in their fabrication and machining [1]. Therefore, other materials, including metal matrix composites, intermetallics, intermetallic matrix composites and ceramic matrix composites, possessing superior high-temperature mechanical properties and oxidation resistance, are currently being investigated. Among these materials, molybdenum disilicide ($MoSi_2$) matrix composites offer a higher strength/density ratio, without decreasing the oxidation resistance.

There are several processing techniques used to produce $MoSi_2$ and its composites. The more conventional routes are based on those employed for ceramics. The procedure is to mix the precursor powders, consolidate the green body into final shape and densify at elevated temperatures. In addition, novel techniques have been developed and proved successful in producing these composites. These include mechanical alloying by high-energy ball-milling, injection moulding, plasma-spraying, vapour infiltration, *in situ* exothermic dispersion (or XD™ process) and combustion synthesis.

Combustion synthesis is a processing technique pioneered by Merzhanov and co-workers in the former Soviet Union during the 1970s. It is a relatively inexpensive and efficient process which, with proper specimen preparation of the elemental powders, leads to products with good mechanical properties from low to high temperatures. The basis of the combustion synthesis process is a self-sustaining exothermic reaction between elemental powders to yield the final product without additional heat. There are two modes for the process: self-propagating high-temperature synthesis mode (SHS) and thermal explosion/combustion mode. In the SHS mode, the reaction is initiated at one end of the sample with the aid of a localized heat pulse that propagates through the pelletized mixture in the form of a combustion wave, leaving behind the reacted product. In the thermal mode, the whole sample is heated uniformly to the ignition temperature whereupon the reaction takes place simultaneously throughout the specimen. This paper describes the processing of $MoSi_2$ composites by the SHS mode of combustion synthesis, and the resulting mechanical properties, including room-temperature hardness, fracture strength, and toughness.

2. Experimental procedure

Commercially available molybdenum (>99.95%), silicon (99.999%) and graphite (99.9995%) powders

* *Present address*: Canada Alloy Castings, Kitchener, Ontario, Canada.

from Johnson Matthey were used in this study. Their particle-size distributions and mean powder sizes were measured by an optical transmission method. The mean particle sizes of the molybdenum, silicon and graphite powders were 5.84, 1.95 and 2.85 μm, respectively.

The powders were weighed and mixed stoichiometrically to produce $MoSi_2$ and $MoSi_2$ composites containing 10 and 20 vol % SiC. The mixtures were ball-milled for 24 h, then uniaxially pressed into cylindrical pellets of 3.81 cm diameter at a pressure of 50 MPa. The samples were typically 35 g in weight, 10 mm thick and of 45%–55% theoretical density. The green density was determined geometrically. The theoretical densities of $MoSi_2$ and SiC are 6.25 and 3.17 Mg m^{-3}, respectively. The theoretical densities of the composites were calculated by the rule of mixtures.

To increase the efficiency of the procedure, the specimens were ignited chemically using a mixture of 50 mol % TiAl and 50 mol % TiB_2. The Al/Ti/B mixture was uniaxially pressed into a disc with a diameter of 23.8 mm and a thickness of 5.0 mm with an applied pressure of 30 MPa. Mo + Si(+ C) compacts were placed on the Al/Ti/B discs and loaded into the furnace. The furnace was heated to 700 °C under 0.1 atm argon. This resulted in ignition and reaction of the Ti/Al/B and subsequently of the Mo/Si/C discs.

The combustion synthesized specimens were coated with a colloidal solution of boron nitride in ethanol to prevent contamination from the graphite die during hot pressing. The hot-pressing cycle consisted of a 1.5 h ramp to a temperature of 1650 °C, a 15 min wait to homogenize the temperature, followed by application of 90 MPa pressure for 1.5 h. All hot pressing was conducted under a vacuum of 1×10^{-4} atm.

Vickers hardness tests were performed on the densified $MoSi_2$ and SiC–$MoSi_2$ composites. The tests were based upon ASTM standard E92-82 [2]. Both the diamond pyramid hardness (kg mm^{-2}) and the Vickers hardness (GPa) were determined.

Rectangular test bars (20 mm × 3 mm × 3 mm) were cut from the polished, hot-pressed pellets with a diamond saw. Five indentations with a 28.4 N load were made uniformly along the length of the polished specimens on the surfaces parallel to the hot-pressed direction. An initial indentation study indicated there was no difference between indentation fractures placed parallel and perpendicular to the hot-pressed direction. Immediately after indentation, the diagonals of the indentations were measured with an optical microscope.

For ambient temperatures, the flexural strength testing standard is based upon MIL-STD 1942(A)-1983 [3] and ASTM C1161-90 [4]. In this study, a fully articulated, four-point-1/4-point flexure test rig was used (Fig. 1) [5].

To minimize fracture-initiating defects such as machining flaws, the samples were machined (Bomas Machine Specialties Inc., Sommerville, MA, USA) to ASTM C1161-90 standards. All specimens were 25 mm long, 3 mm wide and 2 mm thick, with an outer span of 20 mm. The crosshead speed employed was 0.0033 mm s^{-1}. The specimens were tested with the tensile surface perpendicular to the hot-pressed direction.

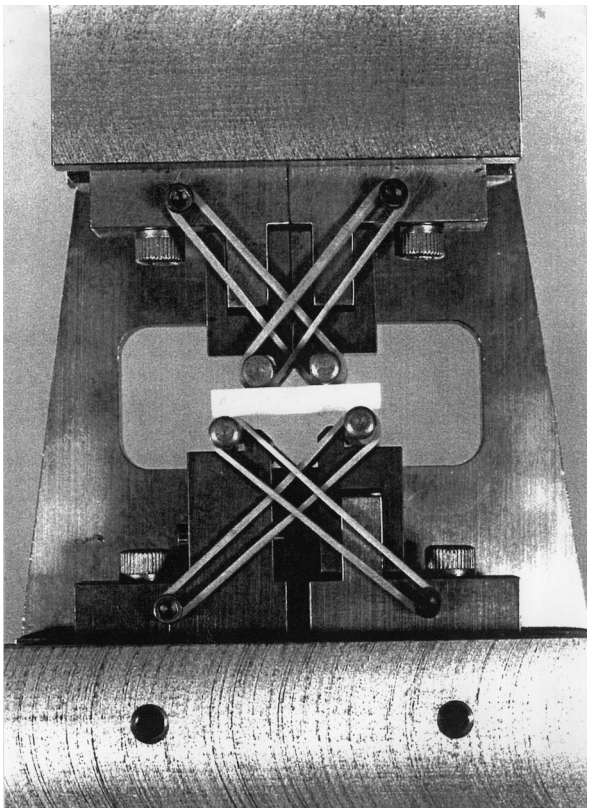

Figure 1 Fully articulated four-point-1/4 point fixture test rig [5].

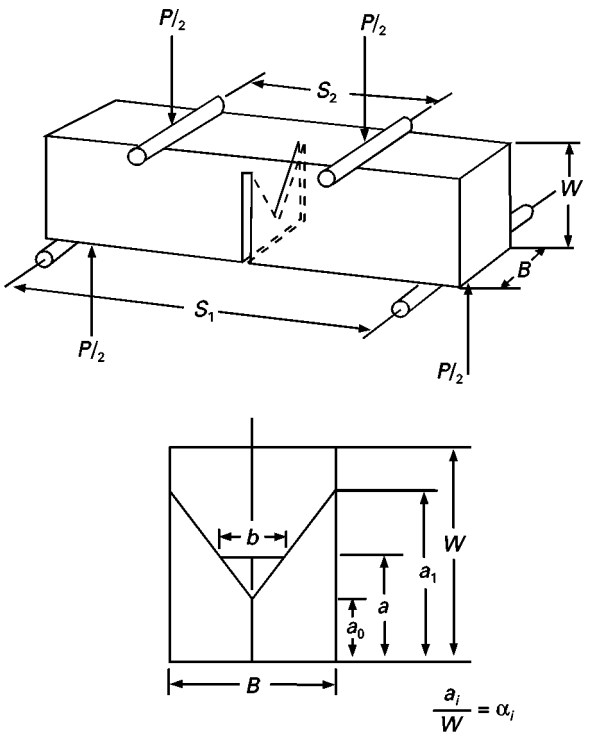

Figure 2 The loading arrangement and the geometry of the four-point-bend chevron-notched bar [7].

The chevron-notched-bend-bar technique was selected to measure fracture toughness [6]. The loading arrangement and geometry of the four-point-bend chevron-notched bar are shown in Fig. 2 [7]. Using

the energy-balance analysis for crack propagation, Munz *et al.* [7] obtained a relationship between the maximum load, P_{max}, and K_{IC} in the stable crack growth regime. The relationship involves a compliance function, Y^*, such that Y^* is minimized to Y_m^* when the load is maximized and

$$K_{IC} = \frac{P_{max}}{B/W^{1/2}} Y_m^* \quad (1)$$

where B is the sample width and W is the sample height. Y_m^* was derived using a straight-through-crack assumption by Munz *et al.* [7], or the slice model of Bluhm [8], as follows

$$Y_m^* = (3.08 + 5.00\,\alpha_0 + 8.33\,\alpha_0^2) \times \left(\frac{S_1 - S_2}{W}\right)\left(\frac{\alpha_1 - \alpha_0}{1 - \alpha_0}\right) \times \left[1 + 0.007\left(\frac{S_1 S_2}{W^2}\right)^{1/2}\right] \quad (2)$$

where $\alpha_0 = a_0/W$, $\alpha_1 = a_1/W$ and the other variables are as defined in Fig. 2 [7]. For the above equation to be valid, stable crack growth must precede final failure, that is, the region between the initial elastic region and the final failure must appear as non-linear on the load–displacement curve [9]. Munz *et al.* [7] and Salem and Shannon [10] have studied the influence of the notch geometry on K_{IC} and have generally agreed that the value of K_{IC} is independent of the chevron geometry (in the range $\alpha_0 = 0.07$– 0.37 and $\alpha_1 = 0.85$ –1.0). The dimensions of the machined specimens were identical to the flexure strength specimen, with the notch geometry as follows: $a_0 = 0.2$ mm and $a_1 = 2.0$ mm ($\alpha_0 = 0.07$, $\alpha_1 = 0.67$). The surface finish of the specimens was obtained using 320 grit abrasive. The specimens were tested with the tensile surface perpendicular to the hot-pressing direction. As a comparison, the toughness of the specimens was measured by the indentation test method proposed by Anstis *et al.* [11]. The fracture toughness was then calculated from the crack lengths radiating from the corners of the Vickers indent by the following relationship

$$K_{IC} = 0.016\left(\frac{E}{H_v}\right)^{1/2} \frac{P}{C_0^{3/2}} \quad (3)$$

where E is Young's modulus (GPa), H_v is the Vickers hardness (GPa), P is the indentation load (N), and C_0 is the crack length (m).

The experimental procedure was similar to that for hardness testing, except that the load was increased to 294 N. Only one load was used, because the toughness has been shown to be load independent for $MoSi_2$ and SiC–$MoSi_2$ composites (i.e. no R-curve behaviour). Immediately after the indentation, the crack length and diagonal of the indentation were measured with an optical microscope at a magnification of $\times 10$. If more than four radial cracks were observed, which occurred often, the four longest orthogonal cracks were assumed to be the primary cracks. These were used for the calculation of H_v and fracture toughness measurements.

Young's modulus, E, and Poisson's ratio, ν, for the materials were calculated using ultrasonic wave velocities measured on the same samples [12]. Because the acoustic wave velocities are influenced by the porosity, Fisher *et al.* [13] proposed extrapolation of the moduli to zero porosity by the following relationship

$$E_0 = \frac{E_\rho}{2\rho - \rho_0} \quad (4)$$

where E_0 is Young's modulus at zero porosity (GPa), ρ is the measured density ($g\,cm^{-3}$), and ρ_0 is the theoretical density ($g\,cm^{-3}$). This value of Young's modulus was used to calculate the fracture toughness.

3. Results

3.1. Characterization of combustion synthesized materials

Some swelling and spalling at the surfaces were observed for the combustion synthesized samples, but in general, the cylindrical shape from the green sample was retained. The densities were measured by the Archimedes method and were found to be in the range of 35%–45% TD, which is lower than the green density. Sections of the samples were analysed using X-ray diffraction. The relative peak intensities and diffraction angles, 2θ, were compared with those prepared from JCPDS (Joint Committee on Powders Diffraction Standards) standards as shown in Figs 3 and 4. The magnified scale of Fig. 4 is used to confirm the presence of SiC. For the unreinforced material, only $MoSi_2$ was present, while the composites contained both $MoSi_2$ and SiC. The SiC peak height increased with the SiC content in the composites. No significant quantities of other phases were observed.

Scanning electron microscopy (SEM) was used to examine the fracture surface to determine the extent of homogeneity and porosity in the synthesized materials as shown in Figs 5 and 6. In the monolithic material, the only distinct features observed were equiaxed and homogeneous $MoSi_2$ grains with a diameter of 5–10 μm. For the composites, two distinct features were observed: fine SiC grains of a few micrometres diameter which surrounded larger $MoSi_2$ grains of 5–10 μm diameter.

3.2. Characterization of hot-pressed materials

The hot-pressed samples were polished to a 0.3 μm alumina powder finish. The densities were measured using the Archimedes method (see Table I). Hot pressing increased the densities of the samples to an acceptable level of 97.5%–98.5% TD.

The samples were etched with a mixture of 15 vol % hydrofluoric acid and 10 vol % nitric acid in distilled water and examined by SEM. The compositional phases of the samples were further analysed by energy dispersive X-ray spectroscopy (EDX) on the SEM. To quantify the X-ray spectra from EDX, a previously

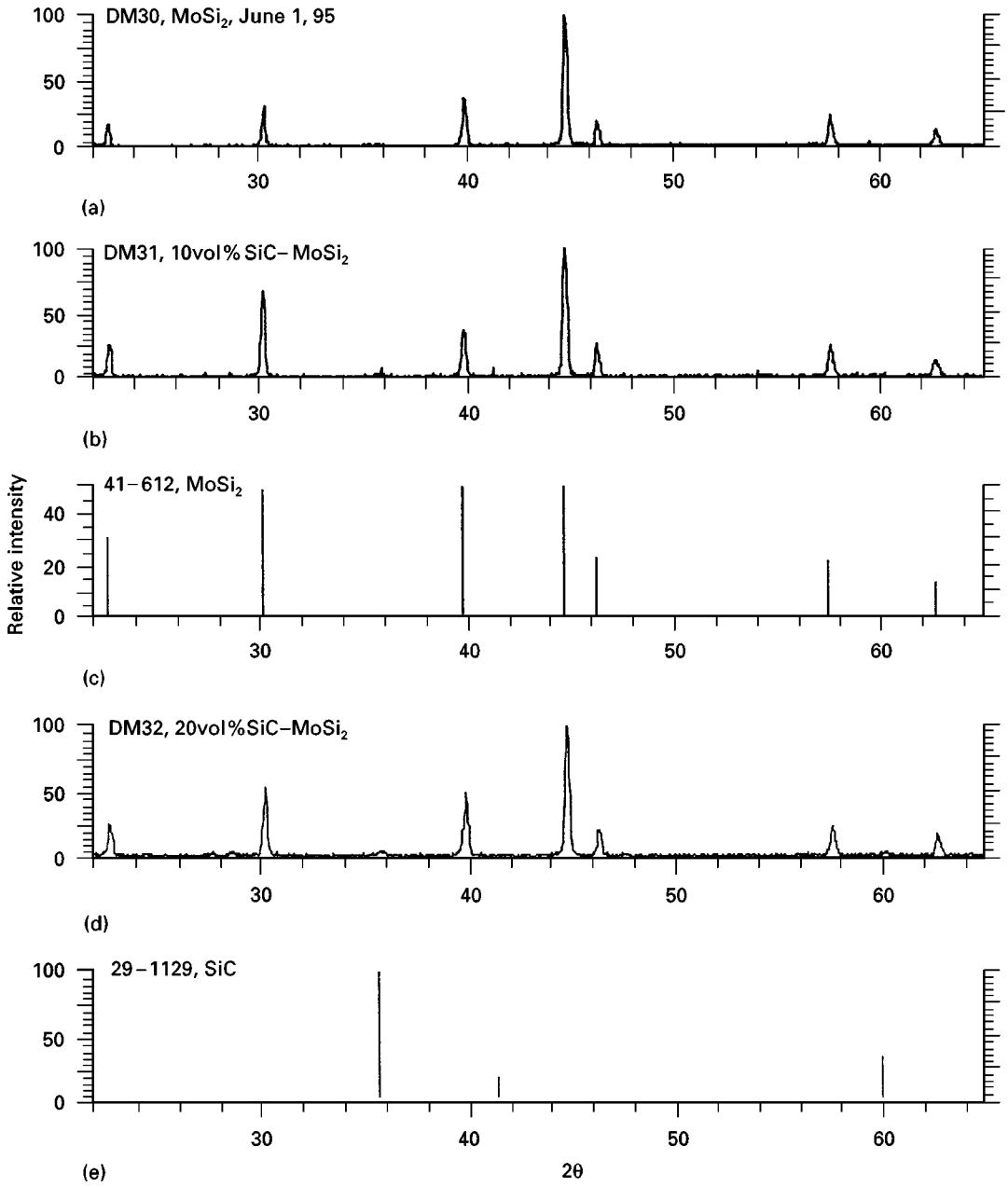

Figure 3 X-ray analysis of combustion-synthesized samples before hot pressing; (a) $MoSi_2$, (b) 10 vol % SiC–$MoSi_2$, (c) $MoSi_2$ reference, (d) 20 vol % SiC–$MoSi_2$, (e) SiC reference.

characterized single crystal of $MoSi_2$ containing regions of Mo_5Si_3 was used. The results are shown in Fig. 7. The grain sizes were determined from scanning electron micrographs of the etched cross-section taken parallel to the hot-pressing direction.

Fig. 8 is a scanning electron micrograph of the polished surface of hot-pressed $MoSi_2$, showing three compositional phases. It was suspected that some of the dark regions were pores and this was confirmed by secondary electron imaging, in which it was observed that the hole edges were brightly "illuminated".

The unilluminated dark regions were solid phases. Qualitative analysis of this region showed the presence of sodium, magnesium, aluminium, silicon, oxygen and calcium as shown in Fig. 8b–f. These are suspected to be impurities from processing and sample preparation. Additional EDX analyses were performed on the elemental molybdenum and silicon powders to determine the source of the oxygen. Elemental oxygen was not found in the molybdenum powder but it was present in the silicon powder, probably as surface SiO_2.

The matrix phase matched the EDX pattern of the standard $MoSi_2$ single crystal. Qualitative analysis of the bright region showed the presence of molybdenum and silicon, which could be unreacted molybdenum and silicon powders. The presence of oxygen in the bright region was not investigated because oxides cause the backscattered electron image to be dark, not bright, due to their non-conductivity. Three different compositional phases were identified in the 10 vol % SiC–$MoSi_2$ composites (Fig. 9). They were analysed by EDX and shown to be $MoSi_2$ (the matrix phase), Mo_5Si_3 (the bright phase) and SiC (the dark phase). Some of the dark phase could also be SiO_2 and porosity.

Fig. 10 shows the etched surface of $MoSi_2$ and 10 vol % SiC–$MoSi_2$. The grain sizes of both $MoSi_2$

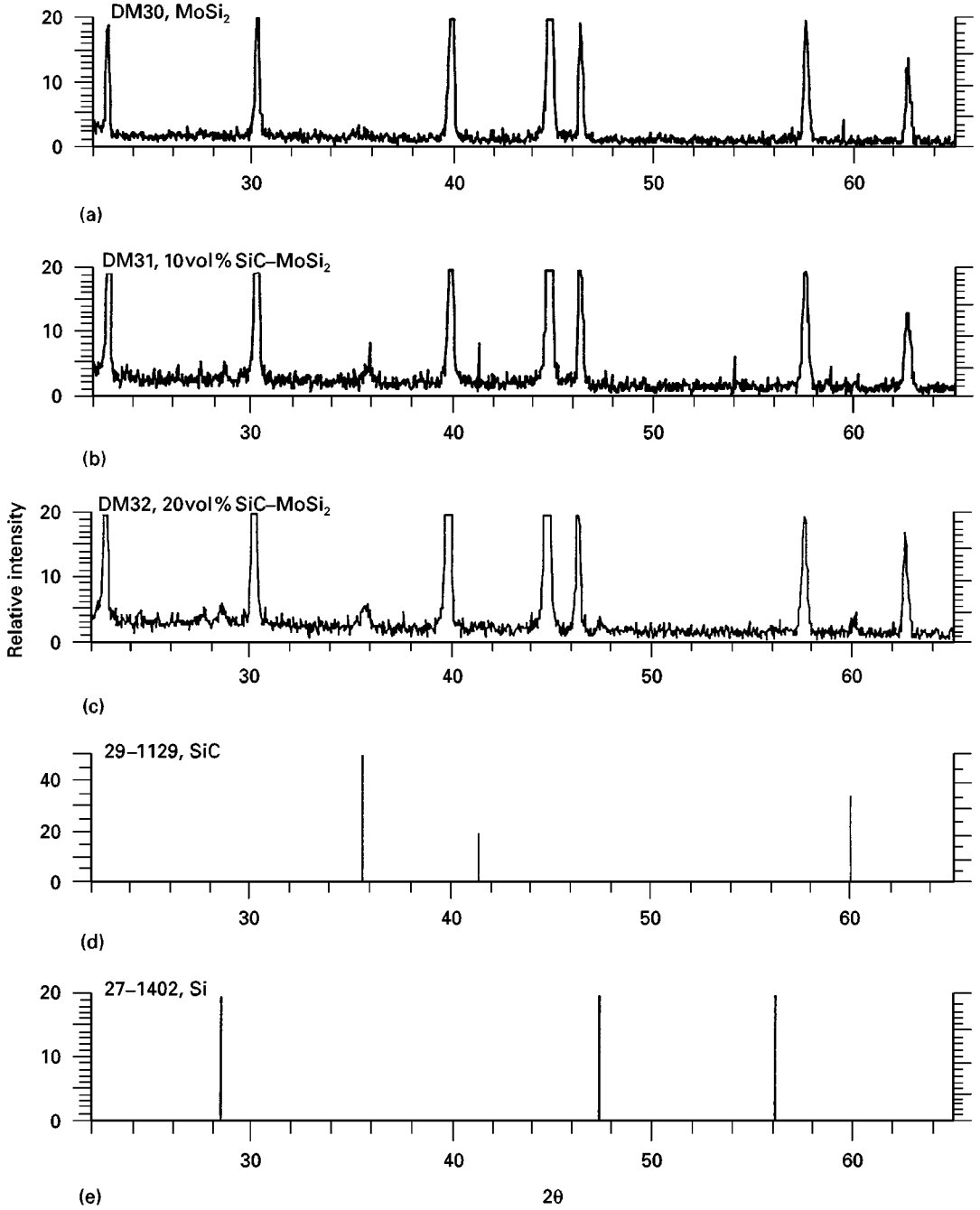

Figure 4 X-ray analysis of combustion-synthesized (a) $MoSi_2$, (b) 10 vol % SiC–$MoSi_2$, (c) 20 vol % SiC–$MoSi_2$, before hot pressing; (d) SiC reference, (e) Si reference.

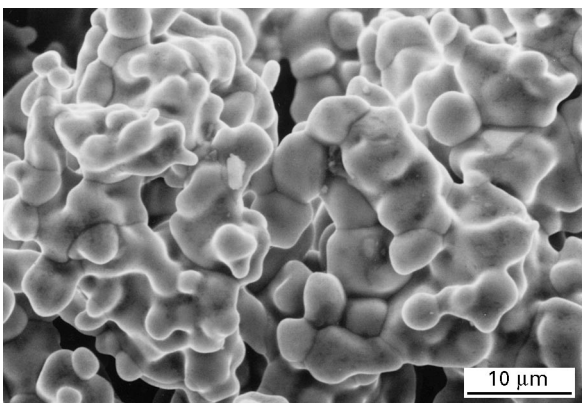

Figure 5 Scanning electron micrograph of the fracture surfaces of $MoSi_2$ (secondary electron mode).

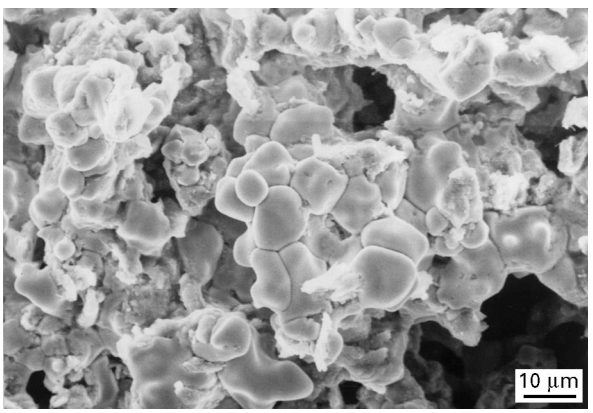

Figure 6 Scanning electron micrograph of the fracture surfaces of 20 vol % SiC–$MoSi_2$ (secondary electron mode).

TABLE I Relative density and grain size of the hot-pressed materials

	$MoSi_2$	10 vol % $SiC–MoSi_2$	20 vol % $SiC–MoSi_2$
Relative density of hot-pressed material	97.0%	97.8%	98.3%
Grain size of Matrix (μm)	21.5	14.0	12.6
Grain size of reinforcement (μm)	–	1–3	3–5

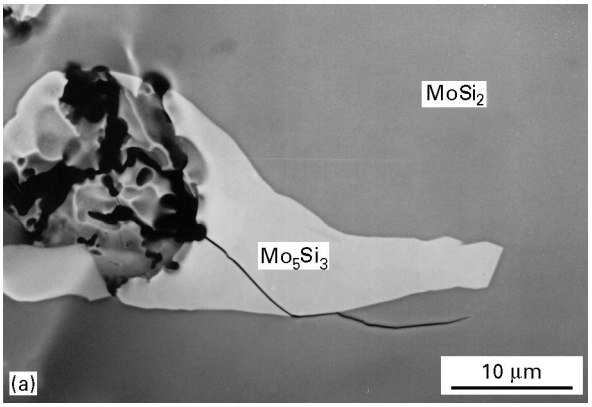

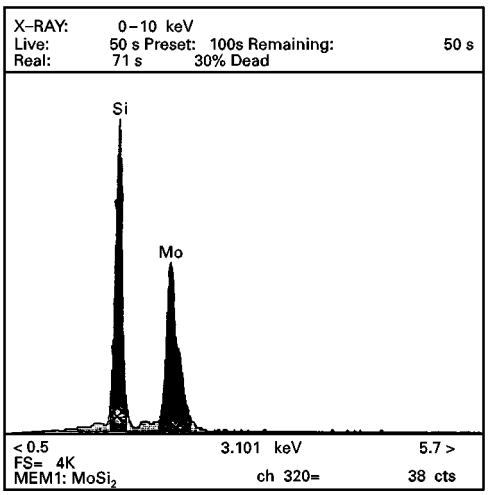

(b)

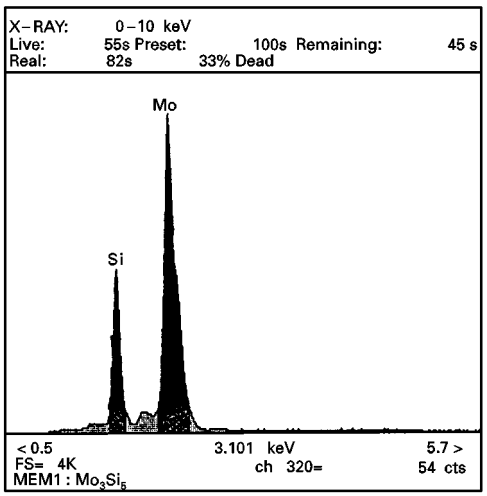

(c)

Figure 7 (a) Scanning electron micrograph of the single crystals of $MoSi_2$ and Mo_5Si_3 (backscattered electron mode), and EDX patterns of (b) $MoSi_2$ single crystal, (c) Mo_5Si_3 single crystal.

and SiC were measured and are listed in Table I. The SiC was distributed uniformly and homogeneously along the grain boundaries of the matrix within the composites.

Microstructurally, the 20 vol % $SiC–MoSi_2$ was similar to the 10 vol % composite (Fig. 11). However, instead of forming fine grains around the $MoSi_2$ grains, the SiC appeared to have clustered together and formed strings of reinforcement.

Table II lists both Vickers hardness and diamond pyramid hardness number for all these materials. The hardness of the materials increased by about 26% following the addition of 20 vol % SiC reinforcement. These results are compared to literature values in Table III. For the monolithic materials, the hardness is slightly higher than that found in the literature (all specimens were hot pressed). For the composites, the hardness values are in close agreement, i.e. within 5% of the data of Jayashankar *et al.* [14] and Bhattacharya *et al.* [15]. However, the hardness of the whisker-reinforced composites [16] was somewhat greater, which is expected because of the more effective load transfer between the matrix and whiskers. It is important to note that in the current study, only a 2.9 kgf load was used, while in the literature, various loads were used. The increase in hardness with SiC addition indicates effective load transfer to the harder SiC-reinforcement due to the strong interface, with no interfacial reaction at the processing temperature [1, 17].

The results of the four-point bend test are shown in Tables IV and V. The strength was 195 MPa for unreinforced $MoSi_2$, increasing by 53% to 299 MPa with 20 vol % SiC reinforcement.

Table V shows various four-point bend test results from the literature. The fracture strength of $MoSi_2$ obtained in this study was generally higher than those reported in the literature, except for Yang *et al.* [18]. For the composites, the strength was in agreement with those reported by other workers, including the results from whisker-reinforced composites. Furthermore, the composite fracture strength of 299 MPa approaches the acceptable regime for structural applications [19].

The fracture toughness data are summarized in Tables VI–IX. Using the chevron-notch test (Tables VI and VII), we observe an increase in fracture toughness from 2.79 $MPa\,m^{1/2}$ for monolithic material to 4.08 $MPa\,m^{1/2}$ for 20 vol % SiC. This represents a 46% incremental increase. The fracture toughness data from the indentation fracture method are summarized in Tables VIII and IX. These are slightly higher than those from the chevron-notch

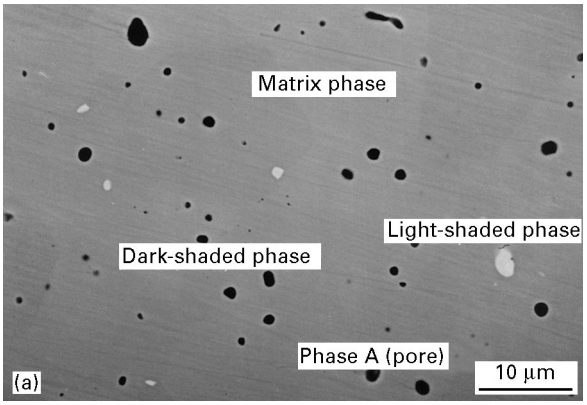

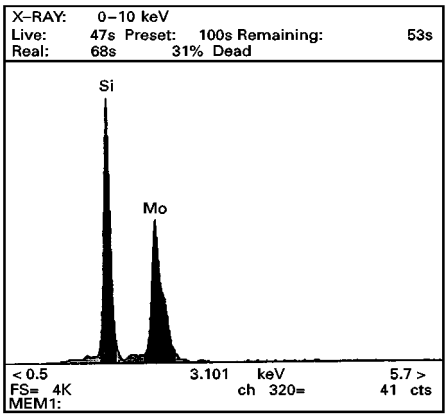

(b)

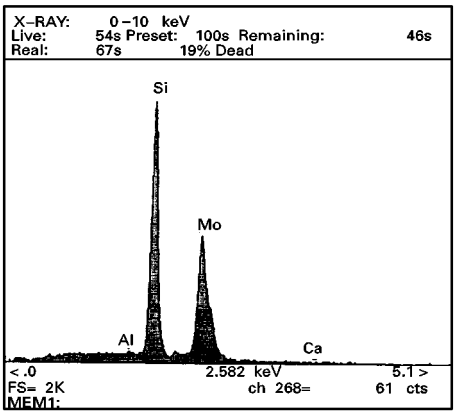

(c)

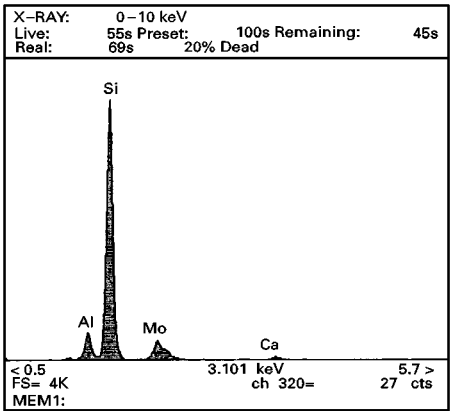

(d)

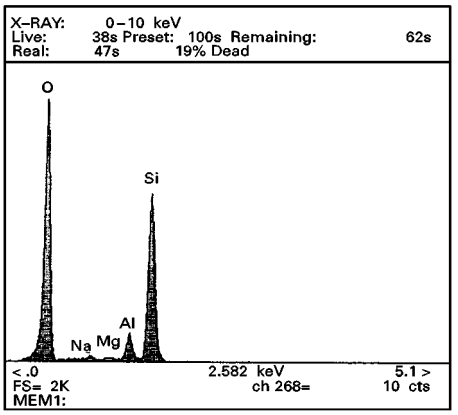

(e)

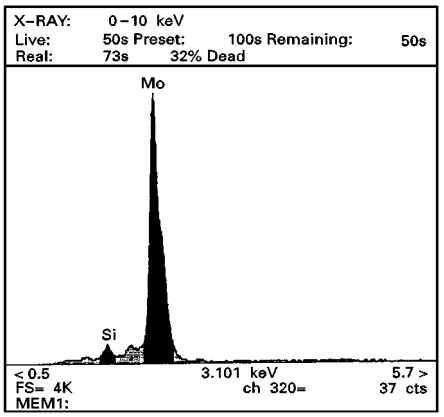

(f)

Figure 8 (a) Scanning electron micrograph of the polished surface of the hot-pressed $MoSi_2$ (backscattered electron mode). EDX spectra of (b) the matrix phase (without light element detector), (c) the matrix phase (with light element detector), (d) the dark phase (without light element detector), (e) the dark phase (with light element detector), and (f) the bright phase (without light element detector).

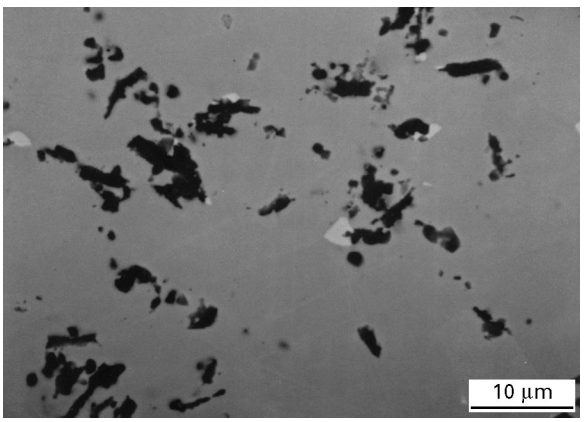

Figure 9 Scanning electron micrograph of the polished surfaces of the 10 vol % SiC–$MoSi_2$ (backscattered electron mode).

method. Moreover, they show a large improvement in toughness, from 2.35 MPa $m^{1/2}$ to 4.98 MPa $m^{1/2}$.

4. Discussion

The flexural strength of the brittle materials is dependent on both its inherent resistance to fracture and the presence of defects. Therefore, analyses of the fracture surface and fractography were done on the specimens to determine the flaws that were responsible for

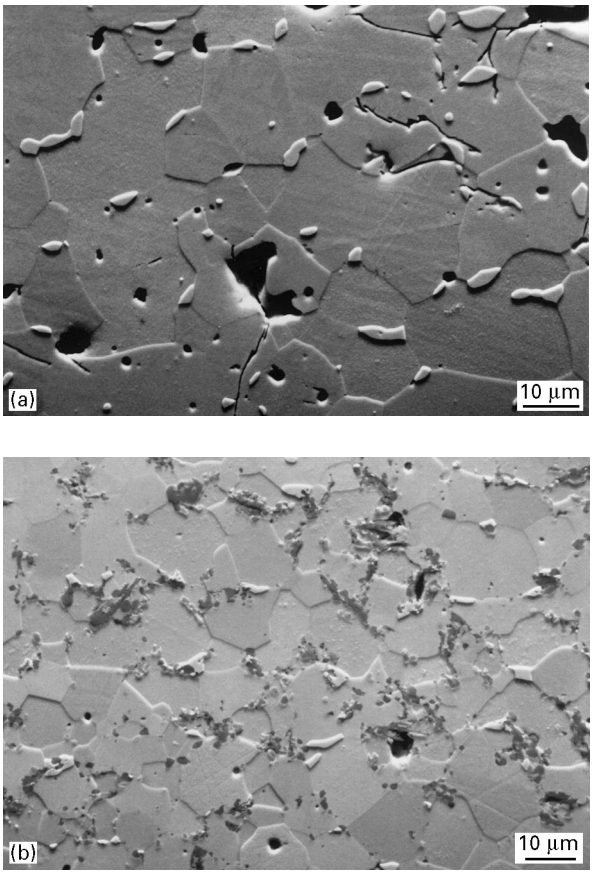

Figure 10 Scanning electron micrographs of the etched surface of (a) $MoSi_2$ and (b) 10 vol % SiC–$MoSi_2$ (combination of secondary electron and backscattered electron modes).

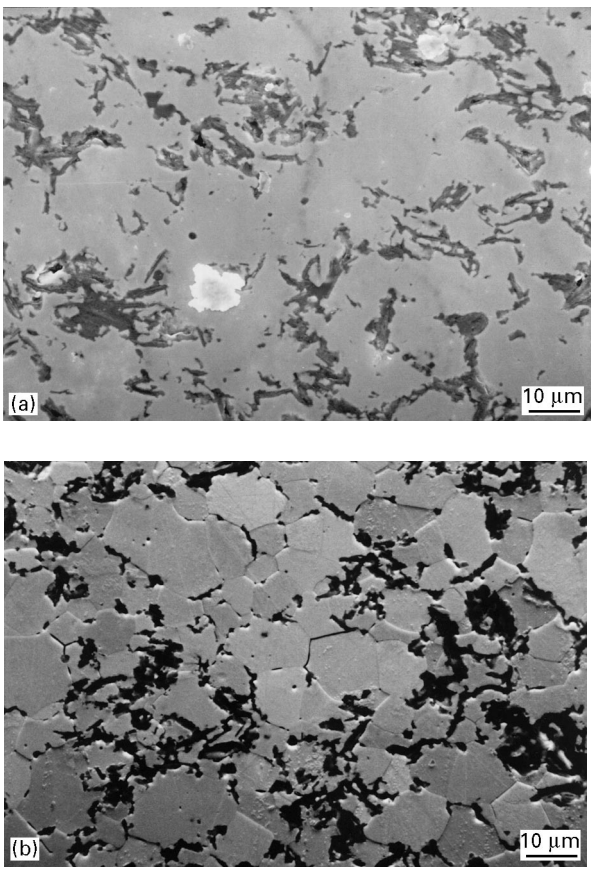

Figure 11 Scanning electron micrographs of (a) the polished surface and (b) etched surface of the 20 vol % SiC–$MoSi_2$ (using a combination of secondary electron and backscattered electron modes).

fracture. The flaw size can be estimated from the fracture strength and the fracture toughness obtained in this study, using the following equations [20, 21].

1. Edge defects

$$K_{IC} = \sigma_f (\pi a)^{1/2} \left(\sec \frac{\pi a}{W} \right)^{1/2} \quad (5)$$

2. Internal defects

$$Y = 1.99 - 0.41 \frac{a}{W} + 18.7 \left(\frac{a}{W} \right)^2 - 38.48 \left(\frac{a}{W} \right)^3 + 53.85 \left(\frac{a}{W} \right)^4 \quad (6)$$

The estimated flaw sizes were 50–60 μm as shown in Table X. Flaws of this magnitude were observed on the fracture surface by SEM. On the fracture surface, transgranular fracture was observed to be the dominant fracture mode for $MoSi_2$ grains (Fig. 12). This mode was also observed by other researchers [17, 22] on specimens produced by the hot-pressing method.

Fig. 13 shows the machining flaws which were detected in only a few samples. On the fracture surface of $MoSi_2$, residual pores from incomplete densification were common as shown in Fig. 14. This is consistent with the lower relative densities of the monolithic materials compared to the composites (Table I). These pores were the major strength-limiting flaws in the monolithic materials.

Pore defects were not significant in the composites, but inhomogeneous grain-size distribution was apparent in both the monolithic materials and the composite materials (Fig. 15). The unusually large grains in these materials may be responsible for initiating fracture. $MoSi_2$ has a tetragonal crystal structure with a high c/a ratio of 2.45. Upon cooling from the densification process, it was subjected to a high anisotropic residual stress within the individual grains. Experimentally, the residual stress in hot-pressed polycrystalline $MoSi_2$ with an 80 μm grain size can be as high as 84 MPa [28]. This large stress will likely cause the materials to fail at a lower fracture stress.

The improved fracture strength of the composite is due to the effective load transfer to the reinforcement by the matrix. Moreover, the SiC reinforcement has a slightly higher elastic modulus than the $MoSi_2$ matrix (see Tables VIII and IX). Unlike combustion synthesis, conventional methods include hot pressing at high temperature for several hours. This treatment causes an interfacial reaction between the SiC-reinforcement and the impurities in the matrix, which leads to a weak interface. Furthermore, these reinforcements tend to oxidize to form a layer of silica which degrades the room-temperature mechanical properties. SiC fibres and platelets are especially susceptible to this condition [17, 29], because both have large contact areas with the matrix.

The strength improvement in the composites can also be attributed to the absence of pores and the reduced amount of SiO_2. Thin layers of SiO_2 can form around each particle, which may isolate the $MoSi_2$ grains, resulting in a weak interface [30], thereby

TABLE II Vickers hardness test results for $MoSi_2$, 10 and 20 vol % SiC–$MoSi_2$

Materials	Number of indentations	Mean Vickers hardness		Standard deviation	
		(GPa)	(kg mm^{-2})	(GPa)	(kg mm^{-2})
$MoSi_2$	5	10.1	(959)[a]	0.1	(13)[a]
10 vol % SiC–$MoSi_2$	5	11.7	(1102)[a]	0.6	(52)[a]
20 vol % SiC–$MoSi_2$	5	12.7	(1199)[a]	0.4	(36)[a]

[a] Diamond pyramid hardness no.

TABLE III Comparison of Vickers hardness results to those obtained in the literature

Materials	This study (GPa)	Chen *et al.* [16] (GPa)	Bhattacharya *et al.* [15] (GPa)	Wade and Petrovic [22] (GPa)	Wade and Petrovic [22] (GPa)	Jayashankar *et al.* [14] (GPa)
$MoSi_2$	10.1	9.9	9.3	8.7	8.92–9.87	8.56
20 vol % SiC–$MoSi_2$	12.7 (p)[a]	13.5–14.7 (w)[b]	12.5–16 (p)[a]			12.5 (p)[a]

[a] Particulate reinforcement.
[b] Whisker reinforcement.

TABLE IV Four-point bend test results for $MoSi_2$, 10 and 20 vol % SiC–$MoSi_2$

Materials	Numer of specimens	Mean flexural stress (MPa)	Standard deviation (MPa)
$MoSi_2$	31	195	39
10 vol % SiC–$MoSi_2$	26	237	39
20 vol % SiC–$MoSi_2$	32	299	43

TABLE VI Fracture toughness results for $MoSi_2$, 10 and 20 vol % SiC–$MoSi_2$ (chevron-notched)

Materials	Number of specimens	Mean fracture toughness (MPa m$^{1/2}$)	Standard deviation (MPa m$^{1/2}$)
$MoSi_2$	6	2.79	0.36
10 vol % SiC–$MoSi_2$	6	3.31	0.41
20 vol % SiC–$MoSi_2$	6	4.08	0.30

resulting in the ineffective rule-of-mixtures strengthening. By *in situ* formation of SiC, carbon will act as a deoxidant and react with silicon to form SiC, minimizing the formation of SiO_2 at the grain boundary [31]. In addition, with the formation of SiC, grain growth in $MoSi_2$ is reduced, hence avoiding residual stresses in the composites.

With a higher hot-pressing temperature, the density can be increased, but at the expense of increasing SiO_2 formation at the interface, which explains the dominance of intergranular fracture. Therefore, the fracture mode gives some indication of a high silica content. Transgranular fracture occurs when the crystal cleavage planes are weaker than the grain boundaries. The weak cleavage planes of $MoSi_2$ are due to the internal stresses on the anisotropic tetragonal unit cell which results from the densification process and a low-energy preferential cleavage plane. This plane runs parallel to the low-energy plane, which is the result of double cross-packed silicon layers alternating with molybdenum layers.

The Weibull modulus, m, and characteristic strength, σ_0, were calculated from the plot in Fig. 16 and tabulated in Table XI. The arithmetic mean strength value (σ at $P = 0.5$), σ_{avg} is usually reported in the literature, and hence, it was calculated here using the following equation ([32] p. 788)

$$\sigma_{avg} = \sigma_0 \, (1/2)^{1/m} \tag{7}$$

Table XI also includes the ratio of the average strength to the characteristic strength to indicate the spread of observed strength values of the materials ([32] pp. 469–90).

TABLE V Comparison of four-point bend test results with those obtained in the literature

Materials	This study (MPa)	Tuffe *et al.* [23] (MPa)	Gibbs *et al.* [24] (MPa)	Yang *et al.* [18] (MPa)	Gac *et al.* [19] (MPa)	Jayashankar *et al.* [14] (MPa)
$MoSi_2$	195	140	173	224	140–160	185
20 vol % SiC–$MoSi_2$	299 (p)[a]		331 (w)[b]	263 (w)[b]	310 (w)[b]	

[a] Particulate reinforcement.
[b] Whisker reinforcement.

TABLE VII Comparison of fracture toughness results to those obtained in the literature (chevron-notched)

Materials	This study (MPa $m^{1/2}$)	Carter *et al.* [25] (MPa $m^{1/2}$)	Richardson *et al.* [26] (MPa $m^{1/2}$)	Gibbs *et al.* [24] (MPa $m^{1/2}$)
$MoSi_2$	2.79	5.32		4.38
20 vol % SiC–$MoSi_2$	4.08	6.59–8.2 (w)[a]	7.5 (pl)[b]	5.68 (w)[a]

[a] Whisker reinforcement.
[b] Platelet reinforcement.

TABLE VIII Fracture toughness results for $MoSi_2$, 10 and 20 vol % SiC–$MoSi_2$ (indentation method)

Materials	Number of indentations	E (GPa)	E_0 (GPa)	ν	H_v (GPa)	Mean fracture toughness (MPa $m^{1/2}$)
$MoSi_2$	5	396	404	0.14	10.1	2.35 ± 0.25
10 vol % SiC–$MoSi_2$	5	396	407	0.15	11.7	3.53 ± 0.46
20 vol % SiC–$MoSi_2$	5	413	422	0.14	12.7	4.98 ± 0.63

TABLE IX Comparison of fracture toughness results with those obtained in the literature (indentation method)

Materials	This study (MPa $m^{1/2}$)	Chen *et al.* [16] (MPa $m^{1/2}$)	Bhattacharya *et al.* [15] (MPa $m^{1/2}$)	Wade and Petrovic [22] (MPa $m^{1/2}$)	Petrovic *et al.* [27] (MPa $m^{1/2}$)	Jayashankar *et al.* [14] (MPa $m^{1/2}$)
$MoSi_2$	2.35	2.4–2.7	2.85	2.3–3.6	2.5	2.5
20 vol % SiC–$MoSi_2$	4.98	3.7–4.8 (w)[a]	4.5 (p)[b]			3.5–4.25 (p)[b]

[a] Whisker reinforcement.
[b] Particulate reinforcement.

TABLE X Estimation of the flaw sizes

Materials (defect)	Fracture strength (MPa)	Fracture toughness (MPa $m^{1/2}$)	Width (mm)	Flaw size (μm)
$MoSi_2$ (edge)	195	2.79	3	65
$MoSi_2$ (internal)	195	2.79	3	62
10 vol % SiC–$MoSi_2$ (edge)	237	3.31	3	62
10 vol % SiC–$MoSi_2$ (internal)	237	3.31	3	50
20 vol % SiC–$MoSi_2$ (edge)	299	4.11	3	60
20 vol % SiC–$MoSi_2$ (internal)	299	4.11	3	48

The low Weibull modulus obtained in this case was most likely due to the flaws mentioned above. However, there was an increase in the modulus with an increase in the amount of reinforcement. With better control of the agglomerates in the original precursor powders, a more uniform, fine-grained material can be produced which allows a stronger and more reliable product.

The results from both fracture toughness methods were in good agreement, which suggests that the values obtained from the chevron-notch test were reliable. However, it should be noted that the indentation method did not yield indentations with idealized four-corner radial cracks. There were radial microcracks along the impression together with a few

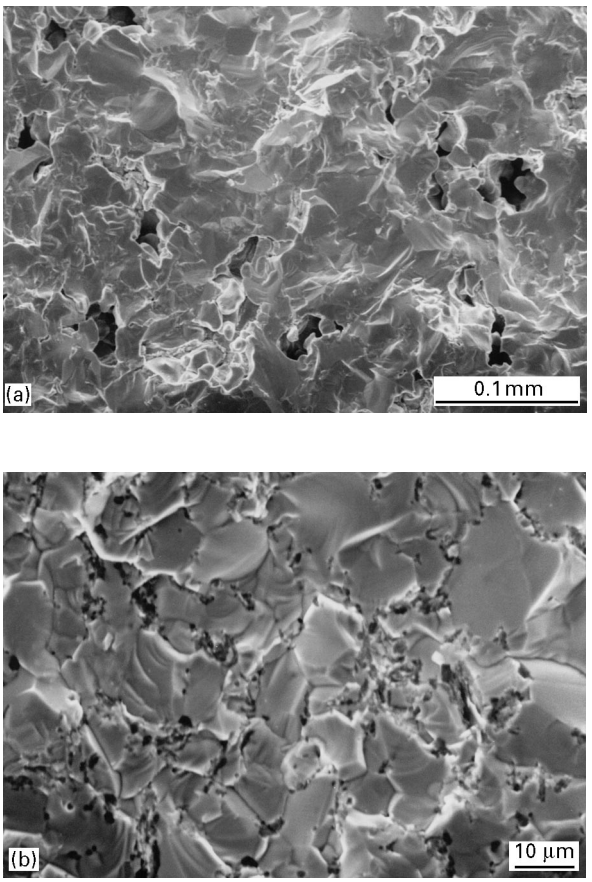

Figure 12 Scanning electron micrographs of typical fracture surface of (a) $MoSi_2$ and (b) 20 vol % SiC–$MoSi_2$ composites.

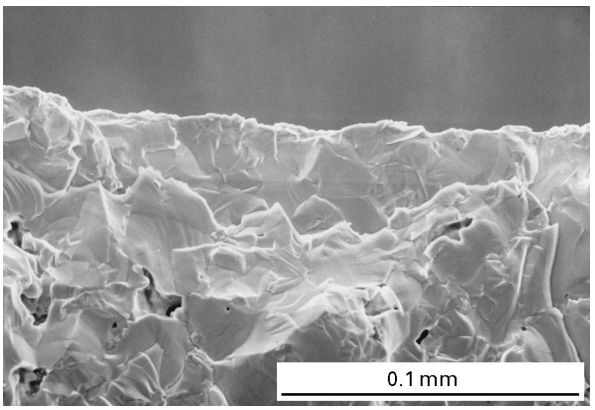

Figure 13 Scanning electron micrograph showing the fracture-initiating machining defect in 20 vol % SiC–$MoSi_2$ composite.

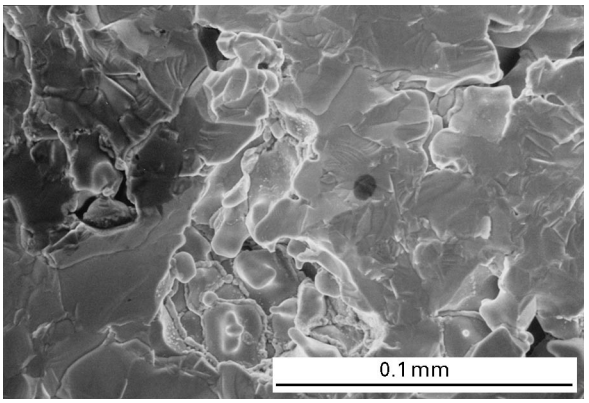

Figure 14 Scanning electron micrograph showing the fracture-initiating pore defect in $MoSi_2$.

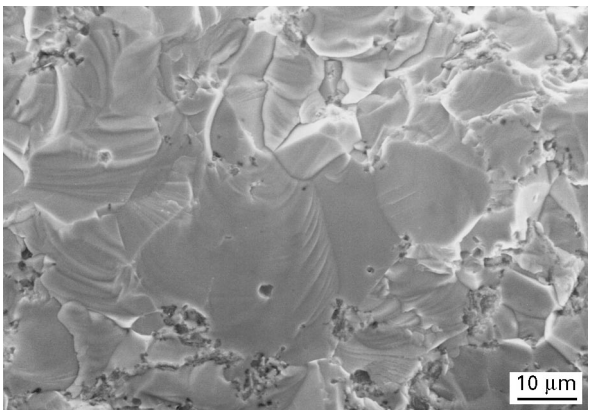

Figure 15 Scanning electron micrograph showing the unusually large grains in 20 vol % SiC–$MoSi_2$ composites.

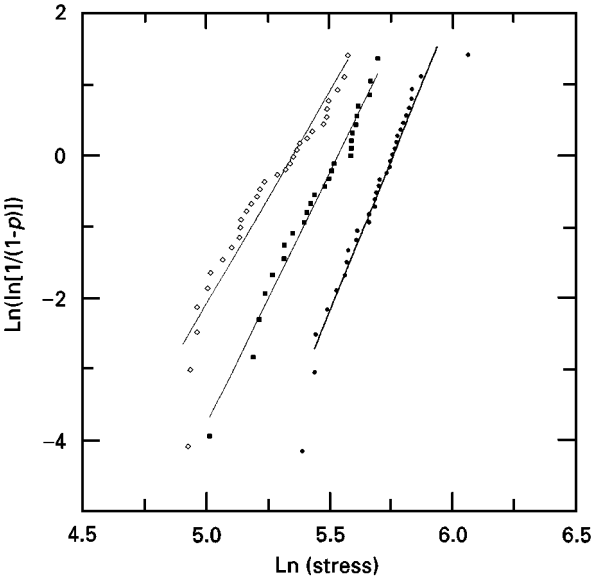

Figure 16 Weibull modulus plots for (◇) $MoSi_2$, (■) 10 and (●) 20 vol % SiC–$MoSi_2$.

shallow lateral cracks which caused chipping and may introduce errors into the fracture toughness calculation. Furthermore, SiC appeared as a dark phase under the microscope, hindering accurate crack measurements.

In summary, there are improvements in all of the room-temperature properties with the addition of SiC reinforcement. The increase in hardness and strength are due to the rule-of-mixtures strengthening effect arising from the strong interface due to low SiO_2 content. The increase in fracture toughness is due to crack deflection along the direction of the weak cleavage plane in $MoSi_2$, and by the net stress field which leads the crack to the tougher reinforcement in order to dissipate its energy.

5. Conclusion

$MoSi_2$ and SiC-reinforced $MoSi_2$ were successfully produced by combustion synthesis. The end product consisted of a $MoSi_2$ matrix and SiC particulate reinforcement. The morphology of the SiC phase varied from particulate to string-like with an increase of SiC content, surrounding the $MoSi_2$ matrix. All the room-temperature mechanical properties tested showed improvement with the introduction of the reinforcement. These results compare favourably with those reported by others using other processing methods, thus showing that this process has potential for the

TABLE XI Results obtained from the Weibull plot

Materials	Number of specimens	σ_0 (MPa)	σ_m (MPa)	σ_0/σ_m	Weibull modulus
$MoSi_2$	31	210	187	1.12	5.95 ± 1.20
10 vol % SiC–$MoSi_2$	26	253	229	1.10	7.05 ± 1.25
20 vol % SiC–$MoSi_2$	32	316	291	1.09	8.45 ± 1.22

fabrication of net-shaped parts for elevated-temperature application.

Acknowledgements

The authors thank Dr N. D. Patel, McMaster University, for the ultrasonic work, and Dr P. H. Boldt, McMaster University, for providing the $MoSi_2$ single crystal.

References

1. A. K. VASUDÉVAN and J. J. PETROVIC, *Mater. Sci. Eng.* **A155** (1992) 1.
2. ASTM E92-82, Standard Test Method for Vickers Hardness of Metallic Materials, in "Annual Book of ASTM Standards", Vol. 15.01 (American Society for Testing and Materials, West Conshahocken, PA) pp. 207–15.
3. MIL-STD 1942(A), "Flexural Strength of High Performance Ceramics at Ambient Temperature, in US Army Military Standard (US Army Materials Technology Laboratory, Waterdown, MA, 1983).
4. ASTM C1161-90, Flexural Strength of Advanced Ceramics at Ambient Temperature, in "Annual Book of ASTM Standards", Vol. 15.01 (American Society for Testing and Materials, West Conshahocken, PA) pp. 333–9.
5. D. M. BLOYCE, M Eng. thesis, McMaster University, Hamilton, Ontario, Canada (1993).
6. J. C. NEWMAN, in "Chevron-Notched Specimens: Testing and Stress Analysis", edited by J. H. Underwood, ASTM STP 855, American Society for Testing and Materials, Philadelphia, PA, 1984, pp. 5–31.
7. D. MUNZ, R. T. BUBSEY and J. L. SHANNON Jr, *J. Am. Ceram. Soc.* **63** (1981) 300.
8. J. L. BLUHM, *Eng. Fract. Mech.* **7** (1975) 593.
9. D. MUNZ, in "Fracture Mechanics of Ceramics", Vol. 5, edited by R. C. Brandt (Plenum, NY, 1983) pp. 457–78.
10. J. A. SALEM and J. L. SHANNON Jr, *J. Mater. Sci.* **22** (1987) 321.
11. G. R. ANSTIS, P. CHANTIKUL, B. R. LAWN and D. B. MARSHALL, *J. Am. Ceram. Soc.* **64** (1985) 533.
12. E. SCHREIBER, O. L. ANDERSON and N. SOGA, "Elastic Constants and Their Measurements" (McGraw-Hill, 1973) p. 6
13. E. S. FISHER, M. H. MANGHNANI, J. F. WANG and J. ROUTBORT, *J. Am. Ceram. Soc.* **75** (1992) 908.
14. S. JAYASHANKAR, S. E. RIDDLE and M. J. KAUFMAN, in "Material Research Society Symposium Proceedings", Vol. 322, edited by C. L. Briant, J. J. Petrovic, B. P. Bewley, A. K. Vasudevan and H. A. Lipsitt (Materials Research Society, Pittsburgh, PA, 1994) pp. 33–40, 71–9.
15. A. K. BHATTACHARYA and J. J. PETROVIC, *J. Am. Ceram. Soc.* **74** (1991) 2700.
16. W. CHEN, W. PASCHETO, A. PANT, R. R. SOOD, R. T. HOLT and R. BERRICHE, in "Proceedings of the 19th Annual Conference on Composites and Advanced Ceramic Materials", Cocoa Beach, FL, *Ceram. Trans.* **56** (1995) 87.
17. J. M. YANG and S. M. JENG, *J. Mater. Res.* **6** (1991) 505.
18. J. M. YANG, W. KAI and S. M. JENG, *Scripta Metall.* **24** (1990) 649.
19. F. D. GAC and J. J. PETROVIC, *J. Am. Ceram. Soc.* **68** (1985) C200.
20. D. BROEK, "Elementary Engineering Fracture Mechanics" (Martinus Nijhoff, Boston, 1982).
21. J. F. KNOTT, "Fundamental of Fracture Mechanics" (Butterworths, London, 1973) pp. 94–149.
22. R. K. WADE and J. J. PETROVIC, *J. Am. Ceram. Soc.* **75** (1992a) 1682.
23. S. E. TUFFE, K. P. PLUCKNETT and D. S. WILKINSON, *Ceram. Eng. Sci. Proc.* **14** (1993) 1199.
24. W. S. GIBBS, J. J. PETROVIC and R. E. HONNELL, *ibid.* **8** (1987) 645.
25. D. H. CARTER, J. J. PETROVIC, R. E. HONNELL and W. S. GIBBS, *ibid.* **12** (1989) 1121.
26. K. K. RICHARDSON and D. W. FREITAG, *ibid.* **14** (1991) 1679.
27. J. J. PETROVIC, R. E. HONELL, T. E. MITCHELL, R. K. WADE and K. J. McCLELLAN, *ibid.* **12** (1991) 1633.
28. J. B. BERKOWITZ-MATTUCK, M. ROSSETTI and D. W. LEE, *Metall. Trans.* **1** (1970) 479.
29. J. J. PETROVIC, *Mater. Sci. Eng.* **A192**/**193** (1995) 31.
30. J. SUBRAHMANYAM, *J. Mater. Res.* **9** (1994) 2620.
31. S. A. MALOY, A. H. HEUER, J. J. LEWANDOWSKI and J. J. PETROVIC, *J. Am. Ceram. Soc.* **74** (1991) 2704.
32. W. D. KINGERY, H. K. BOWEN and D. R. UHLMANN, in "Introduction to Ceramics", 2nd Edn (Wiley-Interscience, NY, 1976).

Received 15 April 1997
and accepted 27 January 1998